



Title	An Evaluation of Reproducibility of the Pacific Decadal Oscillation in the CMIP3 Simulations
Author(s)	Oshima, Kazuhiro; Tanimoto, Youichi
Citation	Journal of the Meteorological Society of Japan, 87(4), 755-770 https://doi.org/10.2151/jmsj.87.755
Issue Date	2009-08
Doc URL	http://hdl.handle.net/2115/39951
Type	article
File Information	JMSJ87-4_p755-770.pdf



[Instructions for use](#)

An Evaluation of Reproducibility of the Pacific Decadal Oscillation in the CMIP3 Simulations

Kazuhiro OSHIMA and Youichi TANIMOTO

Faculty of Environmental Earth Science, Hokkaido University, Sapporo, Japan

(Manuscript received 30 September 2008, in final form 6 March 2009)

Abstract

Reproducibility of the Pacific Decadal Oscillation (PDO) is evaluated in the sea surface temperature (SST) anomaly field in “the 20th century climate in coupled models” (20C3M) simulations of the 24 CMIP3 models. In this evaluation, we examine how well patterns of the PDO match between the observations and simulations by calculating a metric of the patterns that is a function of their spatial correlation and their standard deviation. Among the CMIP3 models, the models with the high PDO metric reproduce the decadal SST variability with opposing polarities between the central North Pacific and the tropical Pacific. As observed, temporal correlation between the PDO and decadal-ENSO indices in those simulations are negatively correlated at the statistically-significant level. The sea level pressure and outgoing longwave radiation anomalies onto the decadal-ENSO index in those simulations are realistic both in the tropical Pacific and North Pacific, indicating that this tropics-extratropics linkage in the SST anomaly field is induced by atmospheric teleconnection. This notion is consistent with the previous studies for the natural climate variability. In contrast, the models with the low PDO metric fail to reproduce those characteristics.

In the simulations under a middle-range IPCC greenhouse gas emissions scenario (A1B), the PDO indices during the 21st century still represent SST variations on the decadal timescales with superimposition on a linear warming trend. Several models which reproduce the observed PDO pattern in the 20th century record tend to simulate a similar pattern over the 21st century. This indicates that the models with the high PDO metric have their own properties that tend to simulate the natural climate variations with the observed pattern under the global warming condition.

1. Introduction

Anthropogenic impacts were detected in surface air temperature (SAT, e.g., Tett et al. 1999; Nozawa et al. 2005), precipitation (Zhang et al. 2007) and moisture content in the atmosphere (Santer et al. 2007) by examining coupled general circulation model (CGCM) simulations forced by observed greenhouse gas and aerosol for the 20th century. Besides the anthropogenic impact, external (solar activity and volcanic eruption) and internal natural variability (e.g., El Niño-Southern Oscilla-

tion, ENSO, Pacific Decadal Oscillation, PDO, and North Atlantic Oscillation, NAO) are involved in observed long-term climate variations. Therefore reproducibility of the long-term natural variability in the CGCMs is important to evaluate the global warming trend by the anthropogenic forcing from the climate variations.

The PDO is one of the most dominant variability of sea surface temperature (SST) on decadal timescales in the North Pacific (Fig. 1) and results in basin-scale changes in SAT, the precipitation and ecosystem in and around the North Pacific (e.g., Trenberth and Hurrell 1994; Mantua and Hare 2002). Associated with the positive (negative) SST anomalies of the PDO in the North Pacific, negative (positive) SST anomalies (Fig. 2a) and positive (negative) outgoing longwave radiation

Corresponding author: Kazuhiro Oshima, Faculty of Environmental Earth Science, Hokkaido University, N10 W 5, Kita-ku, Sapporo 060-0810, Japan.
E-mail: kaz@ees.hokudai.ac.jp
© 2009, Meteorological Society of Japan

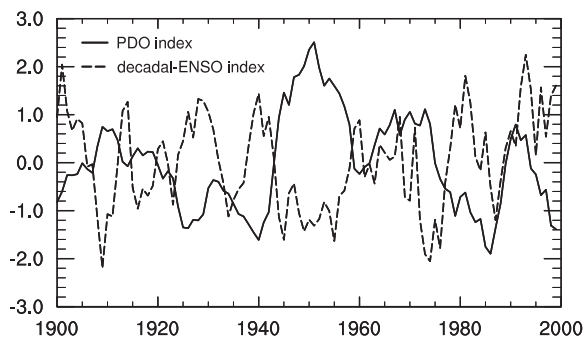


Fig. 1. Time-series of the observed PDO (solid line) and decadal-ENSO indices (dashed line) from 1900 to 1999. The PDO and decadal-ENSO indices are defined as area averaged SSTA over the central North Pacific ($30^{\circ}\text{--}45^{\circ}\text{N}$, $150^{\circ}\text{E--}150^{\circ}\text{W}$, dashed inset box in Fig. 2a) and over the tropical Pacific ($5^{\circ}\text{S--}5^{\circ}\text{N}$, $170^{\circ}\text{--}120^{\circ}\text{W}$, dashed inset box in Fig. 2b), respectively. These indices are normalized by their temporal standard deviations. Temporal correlation coefficient between the two indices is -0.53 .

(OLR) anomalies were observed in the tropical Pacific (Nitta and Yamada 1989; Trenberth 1990; Zhang et al. 1997). These results suggest a linkage of the SST variability between the extratropics and the tropics via changes in the atmospheric circulation. Lau (1997) and Alexander et al. (2002) proposed a role of the atmospheric teleconnection pattern in the North Pacific induced by the tropical SST variability on the decadal timescales using atmospheric general circulation models (AGCM), supporting the observed tropics-extratropics linkage. While air-sea interaction in the mid-latitudes (e.g., Latif and Barnett 1994; Tanimoto et al. 2003; Wu et al. 2003) and/or ocean dynamical processes (e.g., Nonaka et al. 2006; Schneider et al. 2002) are involved in the PDO, we will examine the tropics-extratropics linkage in the CGCMs as the first step on the evaluations of the reproducibility of the PDO.

Outputs of the CGCM simulations conducted by seventeen international institutes are available. Those datasets are archived by PCMDI (Program for Climate Model Diagnosis and Intercomparison) as the World Climate Research Programme's (WCRP's) Coupled Model Intercomparison Project phase 3 (CMIP3). The CMIP3 model simulations are conducted for the Fourth Assessment Report

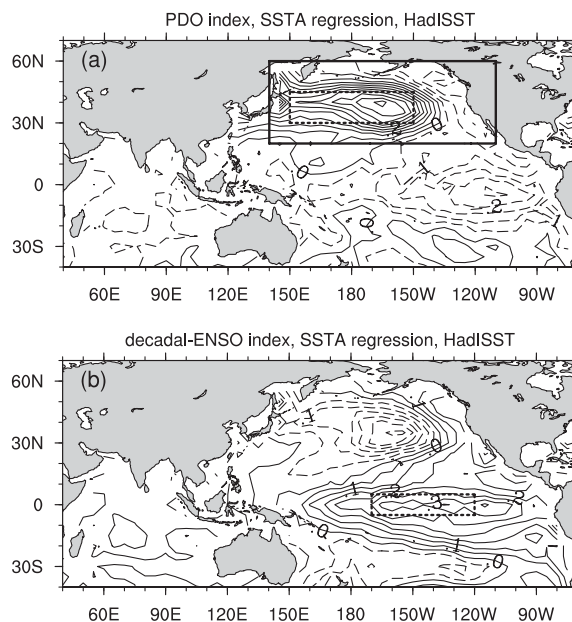


Fig. 2. Regressed SSTA onto the observed (a) PDO index and (b) decadal-ENSO index. Solid and dashed lines denote positive and negative values, respectively. Contour interval is 0.05°C . Dashed inset box over the central North Pacific ($30^{\circ}\text{--}45^{\circ}\text{N}$, $150^{\circ}\text{E--}150^{\circ}\text{W}$) and that over the tropical Pacific ($5^{\circ}\text{S--}5^{\circ}\text{N}$, $170^{\circ}\text{--}120^{\circ}\text{W}$) represent the area for the PDO and decadal-ENSO indices, respectively. Solid line box ($20^{\circ}\text{--}60^{\circ}\text{N}$, $140^{\circ}\text{E--}110^{\circ}\text{W}$) indicates the area for the evaluation of the PDO metric.

of the Intergovernmental Panel on Climate Change (IPCC AR4, IPCC 2007). Using “the 20th century climate in coupled models” (20C3M) simulations, Overland and Wang (2007) evaluated the reproducibility of the PDO. They calculated a spatial correlation between observed and model-simulated PDO spatial patterns and compared their temporal standard deviations. Among the eighteen CMIP3 models, they evaluated that ten models reproduced the PDO patterns in the first modes of empirical orthogonal function (EOF) in the 20C3M simulations. While the first modes of the EOF in the 21st century simulations show a pronounced upward trend, the second modes depict the similar spatial pattern of the PDO.

In the present study, we evaluate reproducibility of the PDO in respect of its spatial pattern and standard deviation for the 20C3M simulations in

Table 1. A list of the 24 CMIP3 models (Models A–X) used in this study. The horizontal and vertical resolution in the atmospheric and oceanic component models, and metrics of the PDO in the 20C3M simulations are shown.

	Model	Atmosphere	Ocean	Metric (20C3M)
A	BCCR-BCM2.0 (Norway)	T63 ($1.9^\circ \times 1.9^\circ$) L31	$0.5\text{--}1.5^\circ \times 1.5^\circ$ L35	0.54
B	CGCM3.1_T47 (Canada)	T47 ($\sim 2.8^\circ \times 2.8^\circ$) L31	$1.9^\circ \times 1.9^\circ$ L29	0.55
C	CGCM3.1_T63 (Canada)	T63 ($\sim 1.9^\circ \times 1.9^\circ$) L31	$0.9^\circ \times 1.4^\circ$ L29	0.50
D	CNRM-CM3 (France)	T63 ($\sim 1.9^\circ \times 1.9^\circ$) L45	$0.5\text{--}2^\circ \times 2^\circ$ L31	0.58
E	CSIRO-MK3.0 (Australia)	T63 ($\sim 1.9^\circ \times 1.9^\circ$) L18	$0.8^\circ \times 1.9^\circ$ L31	0.46
F	CSIRO-MK3.5 (Australia)	T63 ($\sim 1.9^\circ \times 1.9^\circ$) L18	$0.8^\circ \times 1.9^\circ$ L31	0.44
G	GFDL-CM2.0 (USA)	$2.0^\circ \times 2.5^\circ$ L24	$0.3\text{--}1.0^\circ \times 1.0^\circ$ L50	0.44
H	GFDL-CM2.1 (USA)	$2.0^\circ \times 2.5^\circ$ L24	$0.3\text{--}1.0^\circ \times 1.0^\circ$ L50	0.54
I	GISS-AOM (USA)	$3^\circ \times 4^\circ$ L12	$3^\circ \times 4^\circ$ L16	0.39
J	GISS-EH (USA)	$4^\circ \times 5^\circ$ L20	$2^\circ \times 2^\circ$ L16	0.17
K	GISS-ER (USA)	$4^\circ \times 5^\circ$ L20	$4^\circ \times 5^\circ$ L13	0.41
L	FGOALS-g1.0 (China)	T42 ($\sim 2.8^\circ \times 2.8^\circ$) L26	$1.0^\circ \times 1.0^\circ$ L16	0.53
M	INGV-SXG (Italy)	T106 ($\sim 1.1^\circ \times 1.1^\circ$) L19	$1\text{--}2^\circ \times 2^\circ$	0.72
N	INM-CM3.0 (Russia)	$4^\circ \times 5^\circ$ L21	$2^\circ \times 2.5^\circ$ L33	0.35
O	IPSL-CM4 (France)	$2.5^\circ \times 3.75^\circ$ L19	$2^\circ \times 2^\circ$ L31	0.44
P	MIROC3.2_hires (Japan)	T106 ($\sim 1.1^\circ \times 1.1^\circ$) L56	$0.2^\circ \times 0.3^\circ$ L47	0.46
Q	MIROC3.2_medres (Japan)	T42 ($\sim 2.8^\circ \times 2.8^\circ$) L20	$0.5\text{--}1.4^\circ \times 1.4^\circ$ L43	0.68
R	ECHO-G (Germany/Korea)	T30 ($\sim 3.9^\circ \times 3.9^\circ$) L19	$0.5\text{--}2.8^\circ \times 2.8^\circ$ L20	0.56
S	ECHAM5_MPI-OM (Germany)	T63 ($\sim 1.9^\circ \times 1.9^\circ$) L31	$1.5^\circ \times 1.5^\circ$ L40	0.59
T	MRI-CGCM2.3.2 (Japan)	T42 ($\sim 2.8^\circ \times 2.8^\circ$) L30	$0.5\text{--}2.0^\circ \times 2.5^\circ$ L23	0.67
U	NCAR-CCSM3 (USA)	T85 ($1.4^\circ \times 1.4^\circ$) L26	$0.3\text{--}1^\circ \times 1^\circ$ L40	0.53
V	NCAR-PCM1 (USA)	T42 ($\sim 2.8^\circ \times 2.8^\circ$) L26	$0.5\text{--}0.7^\circ \times 1.1^\circ$ L40	0.68
W	UKMO-HadCM3 (UK)	$2.5^\circ \times 3.75^\circ$ L19	$1.25^\circ \times 1.25^\circ$ L20	0.67
X	UKMO-HadGEM1 (UK)	$\sim 1.3^\circ \times 1.9^\circ$ L38	$0.3\text{--}1.0^\circ \times 1.0^\circ$ L40	0.45

the 24 CMIP3 models. Our focus of the evaluations is on a tropics-extratropics linkage and its role on the reproducibility of the PDO. We also see the linkage and its role under the global warming condition.

In the rest of the paper, Section 2 introduces datasets and evaluation method. Section 3 shows the reproducibility of the PDO and the relationship between the PDO and the tropical climate variability in the 20C3M simulations among the 24 CMIP3 models. Section 4 examines the PDO in the 21st century under the global warming condition. Finally, Section 5 is summary.

2. Data and evaluation method

a. Data

We employed the 20C3M simulations from 1900 to 1999 and A1B simulations from 2000¹ to 2099 under a middle-range IPCC greenhouse gas emissions scenario (A1B), based on the 24 CMIP3 models (Table 1, Meehl et al. 2007). For simplicity, we named Model A to X as listed in Table 1 and

¹ Several models start the A1B simulation in 2001 or 2004.

hereafter employ these names. Monthly products of SST, sea level pressure (SLP) and OLR in those simulations were analyzed. Among the CMIP3 models, spatial resolution is various in the atmosphere and ocean, respectively (Table 1). Hence grid points were bilinearly interpolated onto 5° longitude \times 5° latitude for all of the models to avoid the systematic bias depending on the resolution in evaluations of the spatial patterns.

We used Hadley Centre sea ice and sea surface temperature (HadISST, Rayner et al. 2003) and Hadley Centre sea level pressure (SLP, Allan and Ansell 2006) for the 100-year observational reference to the 20C3M simulations. Though a limited period in the satellite era from 1975 onward, NOAA interpolated OLR (Liebmann and Smith 1996) was also available at monthly intervals. Those monthly products were bilinearly interpolated onto $5^\circ \times 5^\circ$.

We calculated monthly climatologies over the 20th century for each of the variables in the observations and 20C3M simulations, respectively. Monthly anomalies as departures from the respective climatologies were averaged over boreal winter (December, January and February). To extract the decadal variability, we removed a linear trend from the 100-year anomaly records and then smoothed them with the 5-year running mean. For the A1B simulations, the monthly climatologies were separately calculated during the 21st century. Then, the anomaly records were processed in the same procedure for the 20th century record.

We defined an area weighted average of the decadal SST anomalies (SSTAs) over the central North Pacific ($30^\circ\text{--}45^\circ\text{N}$, $150^\circ\text{E}\text{--}150^\circ\text{W}$, dashed inset box in Fig. 2a) as PDO index. This area for the PDO index is a center of action in the observed PDO pattern in the first mode of EOF (e.g., Mantua and Hare 2002, Overland and Wang 2007). The large variances of decadal SST variations in the North Pacific are found in this area for the PDO index both in the observation and CMIP3 model simulations. To represent the decadal SST variability in the tropical Pacific, we defined an area weighted average of the SSTAs over the eastern-central tropical Pacific ($5^\circ\text{S}\text{--}5^\circ\text{N}$, $170^\circ\text{--}120^\circ\text{W}$, dashed inset box in Fig. 2b) as decadal-ENSO index. This area is referred to as the Niño3.4 region, commonly used for representing SST variability associated with the ENSO (e.g., Trenberth 1997) and its long-term variations. The large variance of decadal SST variation in the tropical Pacific is found in this area

both in the observation and 20C3M simulations. While the area for the decadal-ENSO index does not correspond to the negative center of action of the regressed SSTA onto the PDO index (Fig. 2a), the significant positive SSTAs regressed onto this decadal-ENSO index cover most of the eastern tropical Pacific (Fig. 2b).

The two indices were normalized by their temporal standard deviation, respectively. Standard deviations of the SSTA over the area for the PDO index and over the area for the decadal-ENSO index in the 20C3M simulations are 0.15 to 0.37°C and 0.08 to 0.58°C , respectively. They correspond roughly to the observed standard deviations that are 0.31°C for the PDO and 0.29°C for the decadal-ENSO, respectively. The simulated decadal SST variance of the regressed SSTA onto the PDO index account for 5–15% and 15–67% of the total SST variance based on the unfiltered and low-pass filtered SST variability in the entire North Pacific (north of 20°N), which is comparable to the observed ratios of 15% and 42%, respectively.

To examine a dominant timescale of the indices, we calculated a power spectrum for the PDO and decadal-ENSO indices in the observation and in the 20C3M simulations. The spectral analysis for the observed PDO index shows a significant peak (above the 90% red noise confidence level) at 20-year and two minor peaks at 9- and 14-year (Fig. 3a). While the spectral peaks of the simulated PDO indices differ from model to model, the dominant variance is found in 10–25 year time scales for each of the simulations (not shown). The ensemble mean of the PDO's power spectrum based on the 24 models presents a large variance in 10–20 year time scales with a significant spectral peak at 20-year above the 90% red noise confidence level (Fig. 3a) because every single model has at least one significant peak in 10–25 year time scales. The spectrum of the observed decadal-ENSO index shows a significant peak at 12.5-year and a minor peak at 25-year (Fig. 3b). As in the simulated PDO indices, the dominant variance of the simulated decadal-ENSO indices is found in 8–20 year time scales, while the individual spectra are different to one another (not shown). As a result, the ensemble mean of the power spectrum of the decadal-ENSO index has much variance 10–20 year time scales with a significant peak at 10-year (Fig. 3b). Therefore, we will apply the 5-year running mean low-pass filter to extract the long-term SST variability associated with the PDO and decadal-ENSO indices.

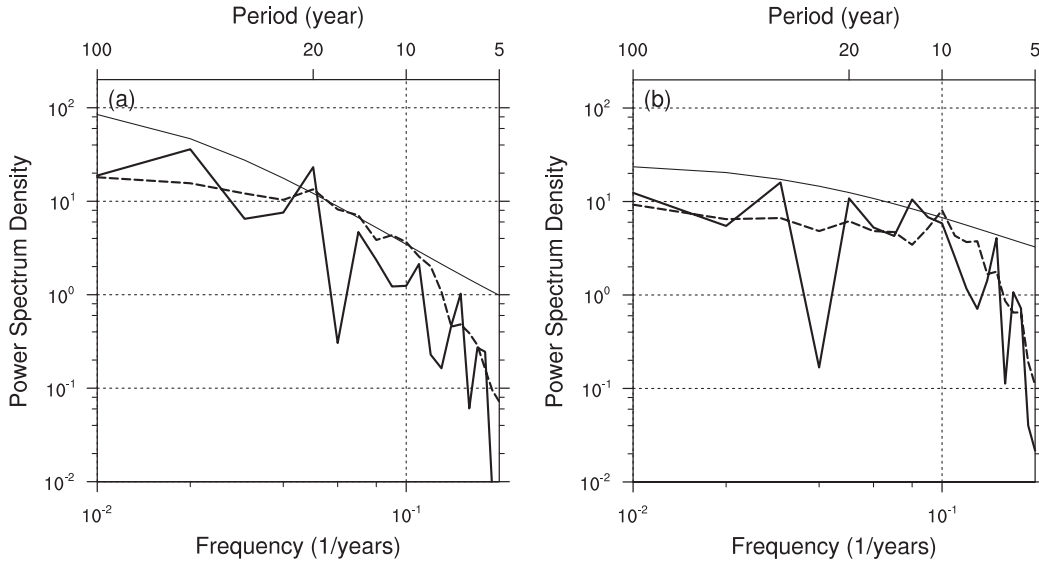


Fig. 3. Power spectrum for the (a) PDO and (b) decadal-ENSO indices in the observation and in the 20C3M simulations. Thick solid lines represent the spectrum of the observed indices. Thick dashed lines represent the ensemble mean of the individual spectrum of the simulated indices based on the 24 models. Thin solid line represents the 90% red noise confidence level.

b. Evaluation method

We calculated the regressed SSTA field of the observation onto the observed PDO index (field r) and that of the 20C3M simulations onto the simulated PDO index (field f). The standard deviation in space of the field f (σ_f) and that of the field r (σ_r) in the North Pacific (20–60°N, 140°E–110°W, solid inset box in Fig. 2a) are defined as:

$$\sigma_f = \sqrt{\frac{1}{N} \sum_{n=1}^N (f_n - \bar{f})^2}, \quad (1)$$

$$\sigma_r = \sqrt{\frac{1}{N} \sum_{n=1}^N (r_n - \bar{r})^2}, \quad (2)$$

where \bar{f} and \bar{r} are the mean values of the regressed SSTAs in the respective area. N is the total number of grid points in the area. The spatial correlation coefficient R_s between the field f and field r in the North Pacific is defined as:

$$R_s = \frac{\frac{1}{N} \sum_{n=1}^N (f_n - \bar{f})(r_n - \bar{r})}{\sigma_f \sigma_r}. \quad (3)$$

These statistics of R_s and σ_f/σ_r are represented in the Taylor diagram (Taylor 2001), as described in Section 3. The Taylor diagram provides useful

information regarding the pattern similarity between the model simulations and the observation, and therefore has been applied to evaluate the reproducibility of the model simulations (e.g., IPCC TAR, IPCC 2001; Kusunoki et al. 2006; AchutaRao and Sperber 2006). Following Taylor (2001), the metric of the PDO (S), which is a measure of its reproducibility in the model simulations, was calculated as follows,

$$S = \frac{4(1 + R_s)^4}{(\sigma_f/\sigma_r + \sigma_r/\sigma_f)^2(1 + R_0)^4}, \quad (4)$$

where R_0 is the maximum correlation attainable. In our evaluations, R_0 is expected to be unity.

3. Reproducibility of PDO in 20C3M simulations

a. Metric

To evaluate and rank the reproducibility of the PDO in the 20C3M simulations of the 24 CMIP3 models, we plotted the R_s and σ_f/σ_r of the individual models in the Taylor diagram as shown in Fig. 4. In the diagram, the azimuthal positions give the spatial correlation coefficient R_s and the radial distance from the origin is proportional to the ratio of the standard deviations σ_f/σ_r . An observational reference point (REF) locates at $\sigma_f/\sigma_r = 1$ on the horizontal line ($R_s = 1.0$) as in Fig. 4. The R_s is greater than 0.6 in most of the models except

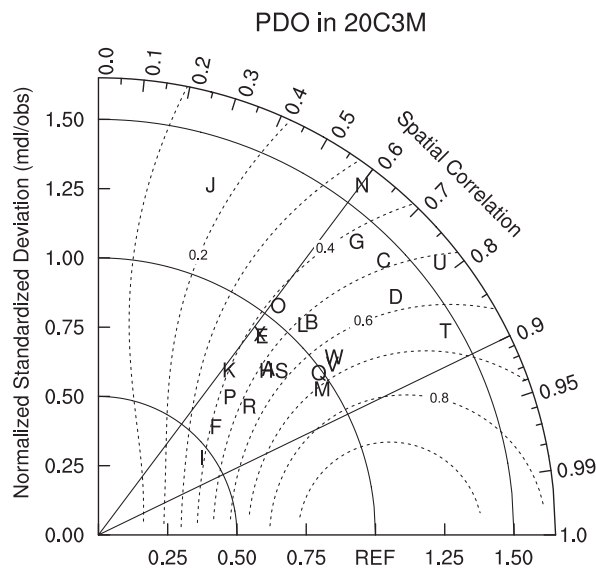


Fig. 4. Taylor diagram for the PDO metric in the 20c3m simulations. Labels of A–X represent the CMIP3 models as listed in Table 1. The azimuthal positions give spatial correlation R_s and the radial distance from the origin is proportional to ratio of standard deviation σ_f/σ_r . An observational reference point (REF) locates at $\sigma_f/\sigma_r = 1$ on the horizontal line ($R_s = 1.0$). Dashed contours denote the PDO metrics.

for the Model J and is greater than 0.7 in 18 models. The σ_f/σ_r is scattered from 0.5 to 1.5 among the models.

The dashed contours in the diagram indicate the metrics of the PDO reproduced in the 20C3M simulations. The metrics of the Models M, V, Q and W are higher than 0.67, because their R_s exceeds 0.8 and σ_f/σ_r are close to the unity. While the σ_f/σ_r of the Model T (1.44) departs from the unity, the metric is high (0.67) due to the highest R_s (0.87) among the models. On the other hand, the metrics of the Models J, N, K and I are less than 0.41, because their R_s tends to be low and σ_f/σ_r depart from the unity. The metrics of the PDO in each of the 20C3M simulations are listed in the last column in Table 1.

In the later sections, we will examine the regressed SSTA patterns onto the PDO and associated tropics-extratropics linkage of the 20C3M simulations with the high (Models M, V, Q, W and T) and low PDO metrics (Models J, N, I and K).

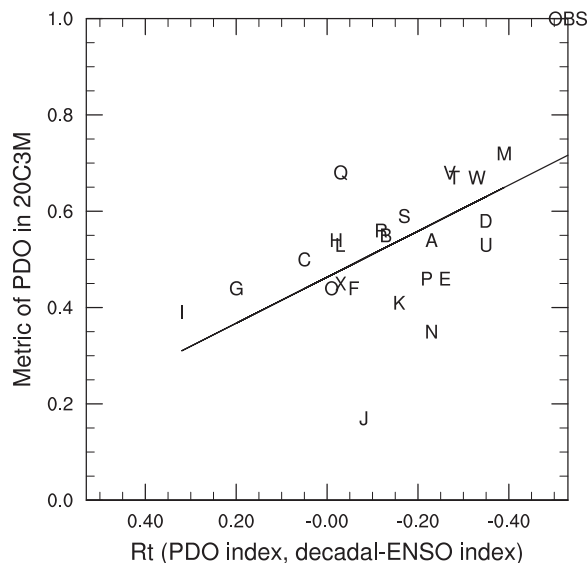


Fig. 5. Scatter plot of the PDO metric and temporal correlation between the PDO and decadal-ENSO indices R_t in the 20C3M simulations (Models A–X). Observational reference point ($S = 1$ and $R_t = -0.53$) is plotted at the upper right corner. Black line indicates the fitting line of least mean square ($S = -0.48 \times R_t + 0.46$). Correlation of the scatter plot is -0.58 above the 99% significant level. Note that horizontal axis is reversed.

b. Reproducibility of PDO and tropics-extratropics linkage

As shown in Fig. 2a, an observational analysis for the 20th century records shows that the regressed SSTAs in the central North Pacific onto the PDO index have opposite polarity to those in the tropical Pacific. The observed PDO index is negatively correlated with the decadal-ENSO index (temporal correlation coefficient $R_t = -0.53$ above the 99% significant level). This coherent horseshoe-like pattern of the regressed SSTAs onto the PDO and statistically-significant R_t have been revealed in the previous studies (Nitta and Yamada 1989; Zhang et al. 1997; Nakamura et al. 1997). However, the correlation R_t between the simulated PDO and decadal-ENSO (horizontal position in Fig. 5) is not always statistically significant in the 24 CMIP3 models (R_t ranges from -0.39 to 0.32). Among the five models with the high PDO metric, four models (Models M, T, V and W) have significant correlation R_t , while the correlation is weaker

for all of the four simulations than for the observation. While the PDO metric is high in the Model Q, the R_t of the Model is nearly zero (-0.03). The correlation R_t in the four models with the low PDO metric is not so high as in the four models with the high PDO metric.

We made a scatter plot of the metrics of the PDO and temporal correlation R_t in the 20C3M simulations (Fig. 5). The observational reference point (the PDO metric = 1 and $R_t = -0.53$) is also plotted at the upper right corner in Fig. 5. A fitting line of the least mean square is $S = -0.48 \times R_t + 0.46$ and the correlation of the scatter plot is -0.58 above the 99% significant level. The Models M, V, W and T with the high PDO metric are plotted in the upper right area of Fig. 5, while the Model Q is plotted far from the fitting line. On the other hand, the Models J, I, N and K with the low PDO metric are plotted in the lower left area or far from the fitting line. Thus the scatter plot implies that the high reproducibility of the tropics-extratropics linkage in the decadal SST variability plays some roles for the high PDO metric in the 20C3M simulations.

We examine the regressed SST, SLP and OLR anomalies in the Indo-Pacific sector of the tropics onto the decadal-ENSO index for the models with the high PDO metric and significant correlation R_t (Models M, V, W and T) and with the low PDO metric and weak correlation R_t (Models J, N, I and K). We also employ the Model Q as an exceptional example because of the high PDO metric but weak correlation R_t .

As expected from the negative R_t in the observed record, the regressed SSTA pattern onto the decadal-ENSO index (Fig. 6a) shows the similar pattern of Fig. 2a but with opposite polarities to one another. In association with the negative SSTAs in the central North Pacific, there is a negative center of action in the observed SLP anomalies in the eastern North Pacific, which act to enhance surface westerlies in the southern part of its center and then cool the underlying upper ocean. In tropics, there is a zonal dipole in the observed SLP anomalies in which positive (negative) anomalies prevail over the western tropical Pacific and Indian Ocean (the central and eastern tropical Pacific, Fig. 6b), respectively, indicative of the weakened Walker circulation in the warm phase of the decadal-ENSO. In this warm phase, the observed OLR anomalies are negative (positive) over the central tropical Pacific (the western tropical Pacific, Fig. 6c). As also revealed in the previous studies,

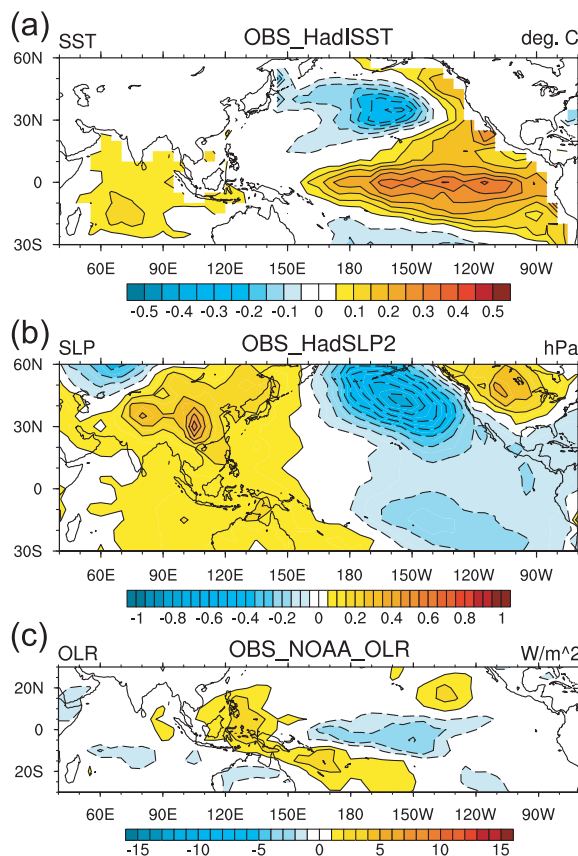


Fig. 6. Regressed (a) SST ($^{\circ}\text{C}$), (b) SLP (hPa) and (c) OLR (W/m^2) anomalies onto the observed decadal-ENSO index. Solid and dash lines denote positive and negative values, respectively. Coloring convention is represented at the bottom in each of the panels.

these results in the observations indicate that the basin-wide warming in the tropical Pacific induces an eastward shift of the convective area and weakens a zonal gradient of the SLP in the tropical Pacific (e.g., Deser et al. 2004; Burgman et al. 2008), and then that these zonal changes in the tropical Pacific (also presented by thick solid lines in Figs. 9a, c, e) induce negative SLP anomalies in the North Pacific via the atmospheric teleconnection (Lau 1997; Alexander et al. 2002) that is involved in the tropics-extratropics linkage of SSTAs.

The regressed SSTAs onto the simulated decadal-ENSO index in the Models M, V, W and T (Fig. 7a) are mostly positive (negative) in the tropical Pacific (the central North Pacific), as expected from their high metrics and significant correlation R_t . As

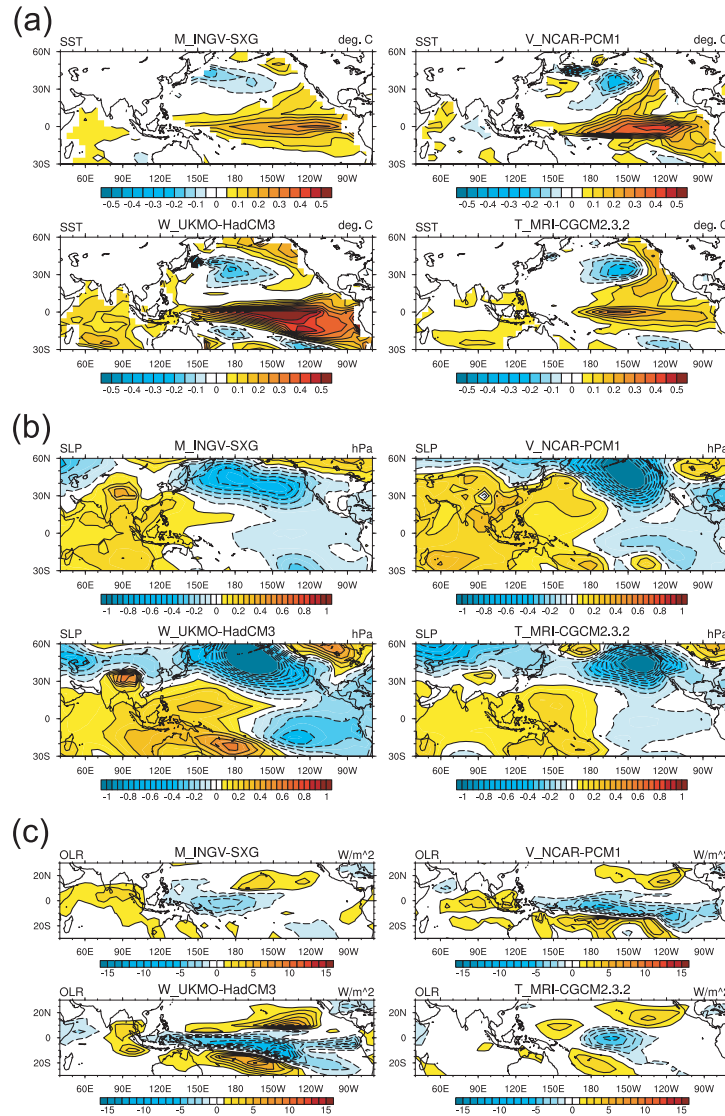


Fig. 7. Same as in Fig. 6, but for the models with the high PDO metric and significant correlation R_t (Models M, V, W and T) in the 20C3M simulations.

observed, there is a zonal dipole in the simulated SLP anomalies in the tropical Pacific as well as a negative center of action in the eastern North Pacific in these four models (Fig. 7b). Coherent negative OLR anomalies around 180°E/W are common in the four models, while the positive anomalies in the western tropical Pacific are not well simulated as observed (Fig. 7c). These results on the simulations with the high PDO metric and the significant correlation R_t indicate that the changes in the OLR and SLP over the tropical Pacific during the warm phase of the simulated decadal-ENSO induce the

atmospheric teleconnection pattern involved in the tropics-extratropics linkage of SSTAs, which is consistent with the observational analysis.

On the other hand, the models with the weak correlation R_t (Models J, N, K, I and Q) fail to reproduce above-mentioned characteristics in the observed SLP and OLR anomalies during the warm phase of the decadal-ENSO (Figs. 8b, c), while they are still successful in simulating the basin-scale warming in the tropical Pacific SSTA field (Fig. 8a). Specifically, a zonal dipole of the SLP anomalies (Fig. 8b) and negative OLR anomalies in these

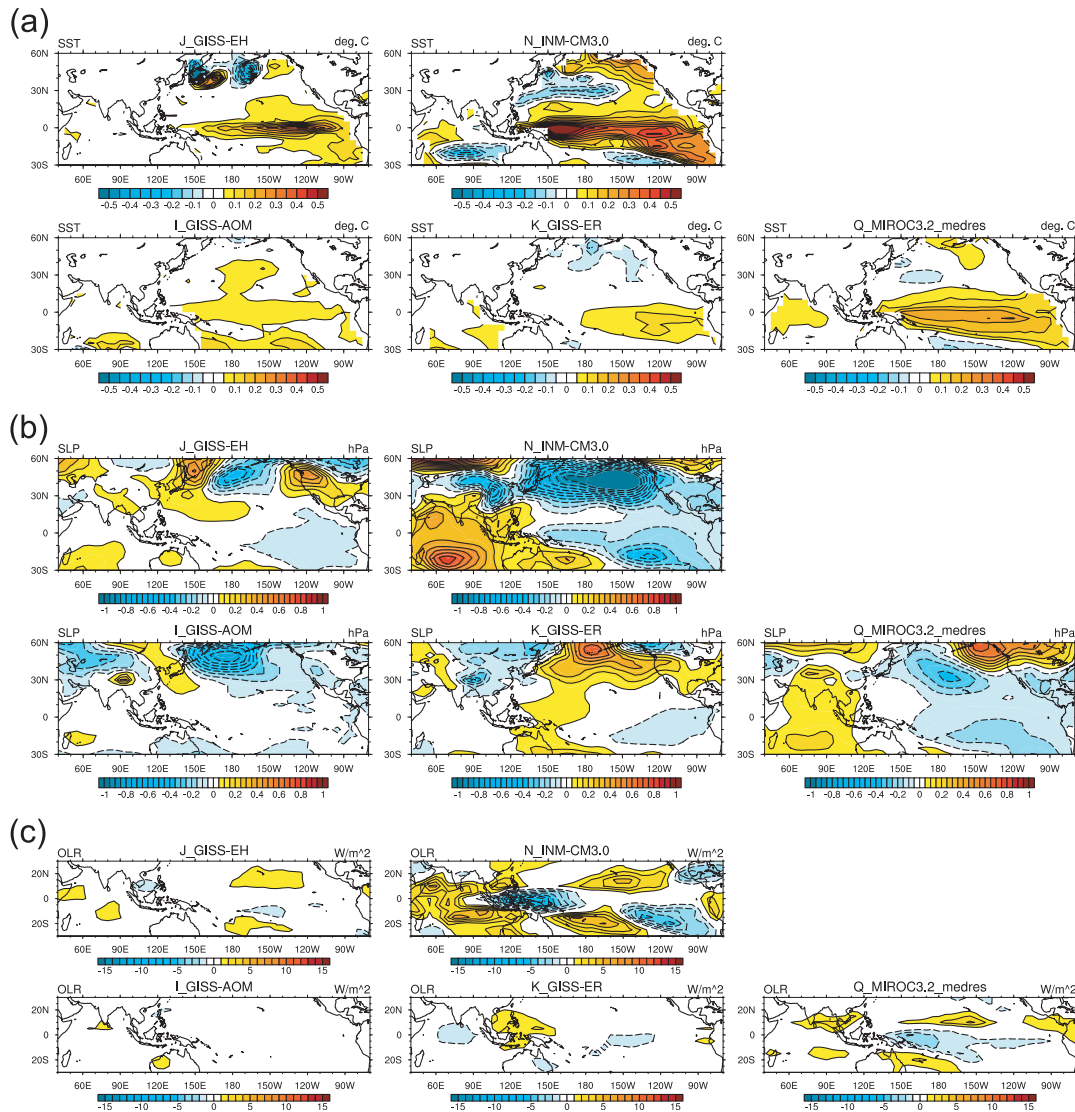


Fig. 8. Same as in Fig. 6, but for the models with the weak correlation R_t (Models J, N, I, K and Q) in the 20C3M simulations.

five models (Fig. 8c) are much weaker in the Models J, I and K or locate at an inappropriate area in the Models N and Q, compared to the observations.

We attempt a closer look at the simulated zonal variations of the SST, SLP and OLR anomalies over the tropical Pacific. An eastward increase in the simulated SSTAs is mostly represented (Fig. 9a) and common in the models with the high PDO metric and significant correlation R_t (Models M, V, W and T). Meanwhile, the increase of the simulated SSTa is much weaker in the Models J, K, I and Q or is anomalously enhanced in the 140°E–

180°E/W sector in the Model N (Fig. 9b). Accompanying these differences in the simulated SSTAs, the four models with the high PDO metric reproduce a zonal dipole of the SLP anomalies in the tropical Pacific as observed (Fig. 9c). However the SLP anomalies over the tropical Pacific are weaker in the Models J, K, I and Q, and emerge in the inappropriate location in the Model N, compared to the observed SLP (Fig. 9d). The negative OLR anomalies around 140°W–180°E/W in the four models with the high PDO metric mostly correspond to the observed anomalies, while the positive

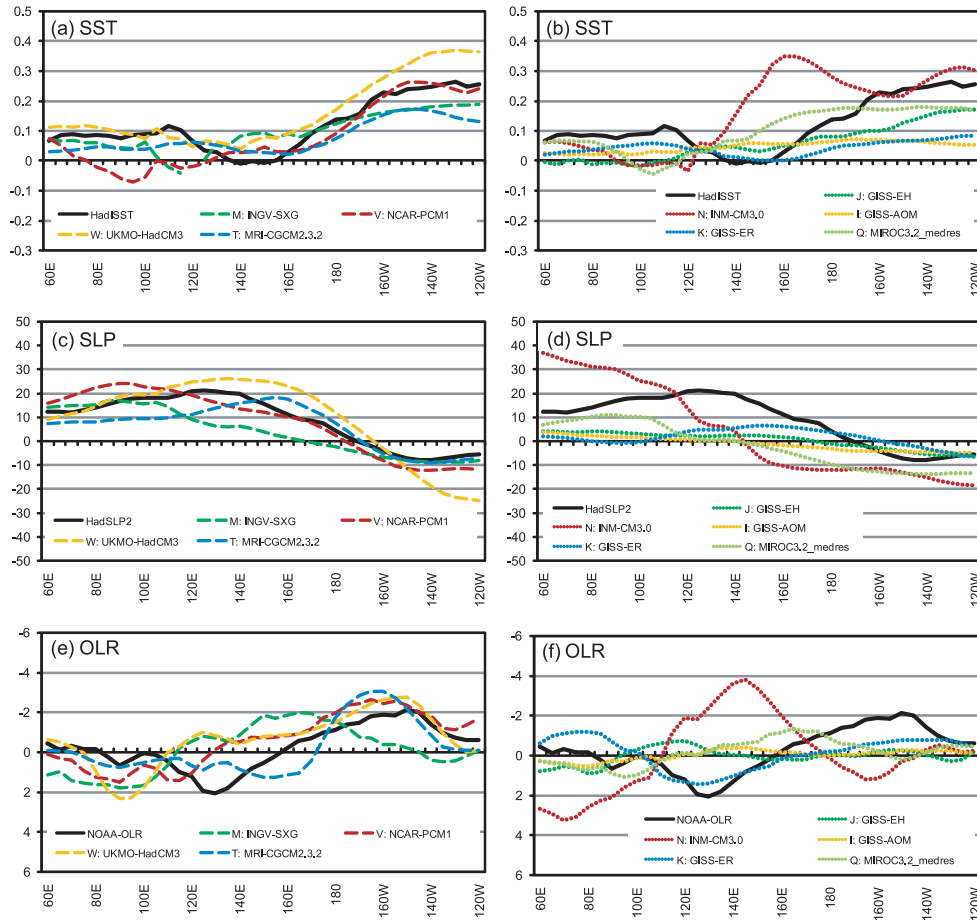


Fig. 9. Zonal plots of (a, b) regressed SST, (c, d) SLP and (e, f) OLR anomalies onto the decadal-ENSO index averaged over 10°S – 10°N in the tropical Pacific. Thick solid line indicates the observed anomalies. Colored dashed lines in the left panels represent the anomalies in the Models M, V, W and T. Colored dot lines in the right panels represent the anomalies in the Models J, N, I, K and Q. Note that the vertical axes of OLR anomalies (e, f) are reversed.

OLR anomalies simulated in the four models emerge around 90 – 110°E , 40° west of the observed (Fig. 9e). The OLR anomalies in the five models with the weak correlation R_t are much weaker (Models J, K, I and Q) or anomalously enhanced in the 120 – 160°E sector (Model N), compared to the observations (Fig. 9f).

Thus the large differences in the simulated SST, OLR and SLP anomalies associated with the decadal-ENSO are found in the tropical Pacific between the models with the high PDO metric and the others. Reproducibility of the zonal variations in the simulated SST, SLP and OLR anomalies over the tropical Pacific associated with the decadal-ENSO is likely needed for the realistic atmospheric

teleconnection pattern that will form the horseshoe-like pattern of the simulated SSTa as in the Models with the high PDO metric and significant correlation R_t .

4. PDO under the global warming condition

In this section, we examine characteristics of the PDO under the global warming condition using the A1B simulations in the same way as conducted for the 20C3M simulations.

Figure 10a shows the 200-year time-series of the area weighted SSTa averaged over the dashed inset box of the central North Pacific in Fig. 2a, based on the 20C3M simulations and A1B simulations. A warming trend in the individual time-series is

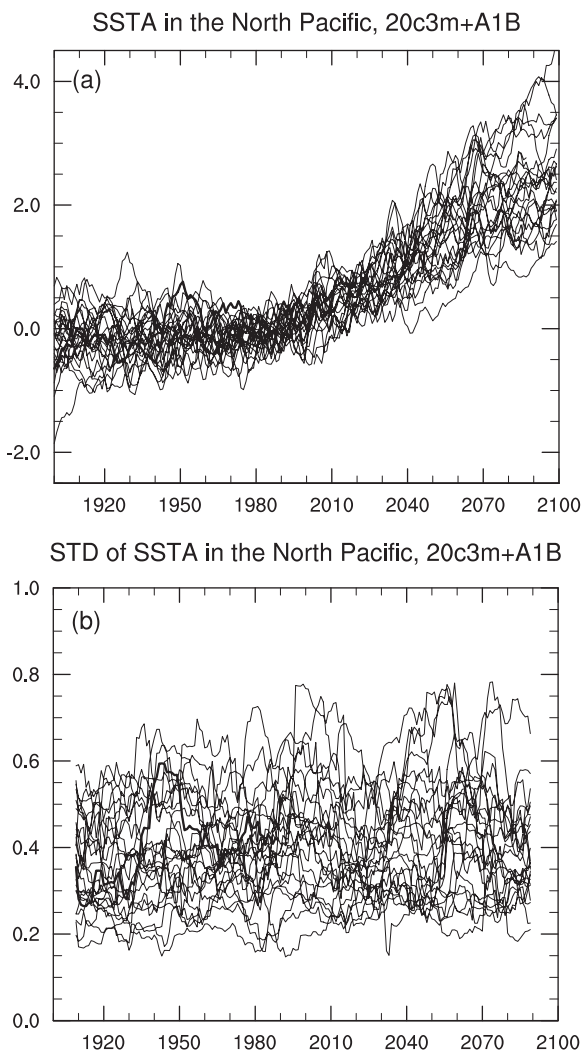


Fig. 10. (a) Time-series of area weighted SSTA averaged over the dashed inset box of the central North Pacific in Fig. 2a from 1900 to 2099 and (b) their temporal standard deviation over the running 20-year window. Thick solid line represents observed time-series over the 20th century. Thin solid lines represent the time-series in the 20C3M and the A1B simulations of the 24 CMIP3 models.

enhanced in the 21st century. An increase rate of the trend over the 21st century varies from 1.1 to 4.0°C/100 years among the 24 CMIP3 models. The indices still represent variations on the decadal timescales in the 21st century with superimposition on the warming trend (Fig. 10a). After removing the linear warming trend from the indices, temporal

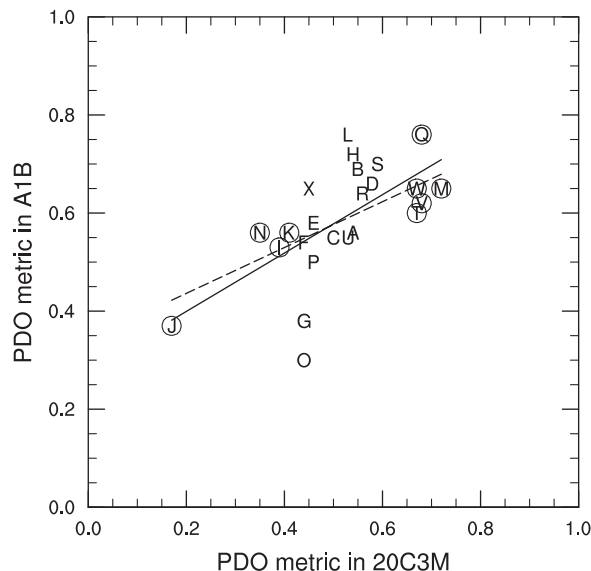


Fig. 11. Scatter plot of the PDO metrics in the A1B simulations and the 20C3M simulations. Black solid and dashed lines indicate fitting lines of least mean square for the 24 CMIP3 models and for nine models marked with circles (Models M, V, W, T, Q, J, N, I and K), respectively. Correlation of the scatter plot for the 24 models is 0.64 above the 99% significant level and that for nine models is 0.87 above the 99% significant level.

standard deviations for the detrended (*i.e.*, residual) PDO indices over the running 20-year windows are calculated. Those standard deviations in the A1B simulations are as much as those in the 20C3M simulations (Fig. 10b). A scatter plot of the increase rates of the trend and standard deviations of the PDO indices during the 21st century for the individual A1B simulations is unlikely to show any dependence between these two statistics (not shown).

To compare regressed SSTA patterns onto the PDO index in the A1B simulations with those in the observation, we calculated the metric of the PDO for the A1B simulations onto the observation as evaluated for the reproducibility of the 20C3M simulations. The spatial correlation coefficient R_s in the A1B simulations is greater than 0.7 in 22 models. The ratios of the standard deviations σ_f/σ_r are scattered from 0.5 to 1.8 among the models. As a result, the metric in the A1B simulations ranges from 0.30 to 0.76 (vertical position in Fig. 11). We made a scatter plot of the PDO metrics in the A1B

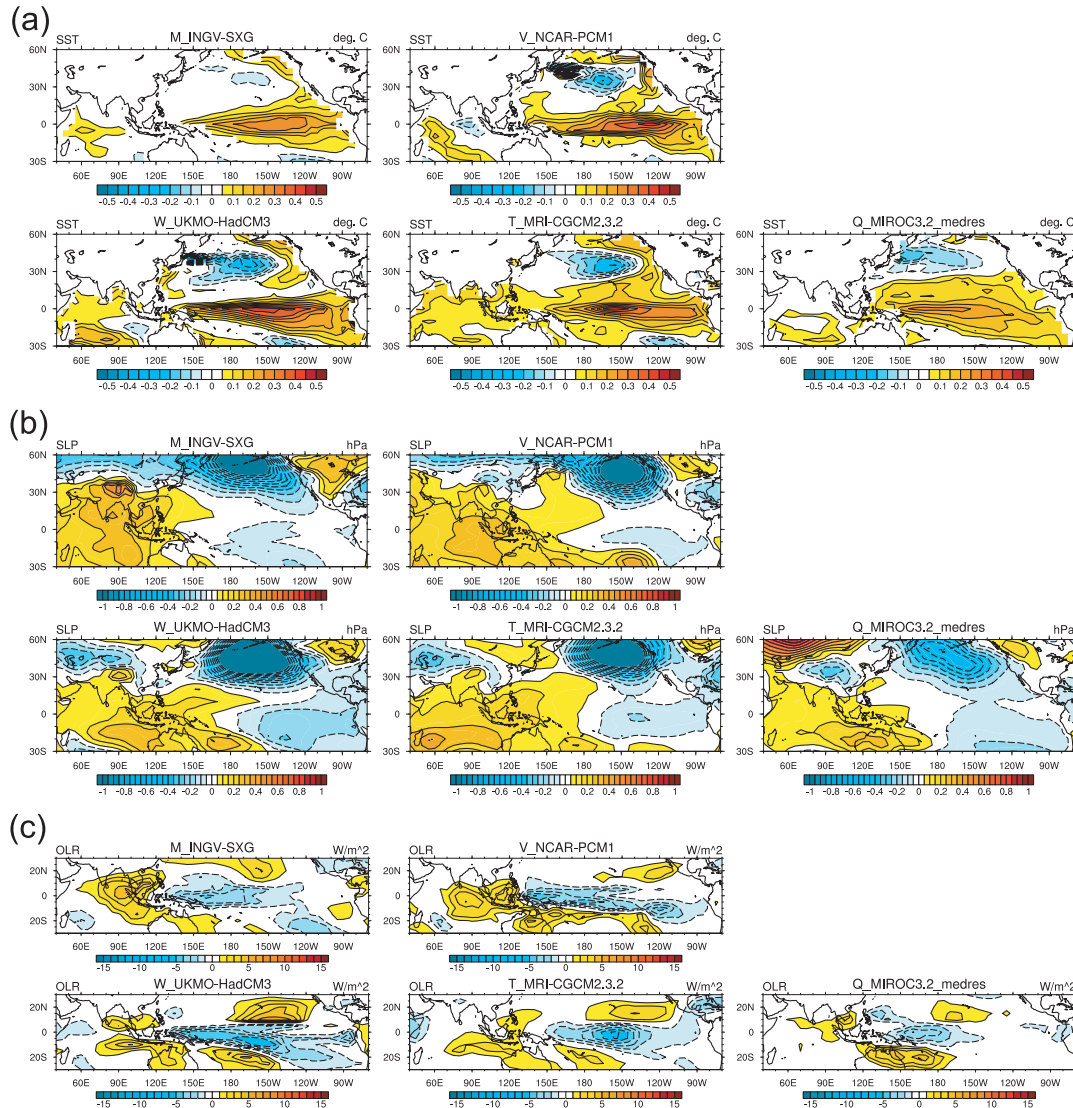


Fig. 12. Same as in Fig. 6, but for the five models with the high PDO metric (Models M, V, W, T and Q) in the A1B simulations.

simulations and those in the 20C3M simulations (Fig. 11). The five models with the high PDO metric in the 20C3M simulations (Models M, V, W, Q and T) are plotted in the upper right area in the scatter plot, while the four models with the low PDO metric in the 20C3M simulations (Models J, N, K and I) are plotted in the lower left area. While a correlation coefficient of the scatter plot based on the 24 CMIP3 model simulations is 0.64 above the 99% significant level, that based on the nine model simulations (Models M, W, V, T, Q, I, J, K and N) is much higher (0.87 above the 99% significant

level). Thus, the model with the higher PDO metric in the 20C3M simulations tends to simulate the similar PDO pattern in the A1B simulations, which is in agreement with the results in Overland and Wang (2007).

As expected from the high PDO metric in the A1B simulations by Models M, V, W, T, and Q, the regressed SSTAs onto the decadal-ENSO index show the horseshoe-like pattern (Fig. 12a). Compared to the 20C3M simulations, negative SST anomalies over the central North Pacific are enhanced in the Model Q, but weakened in the Model

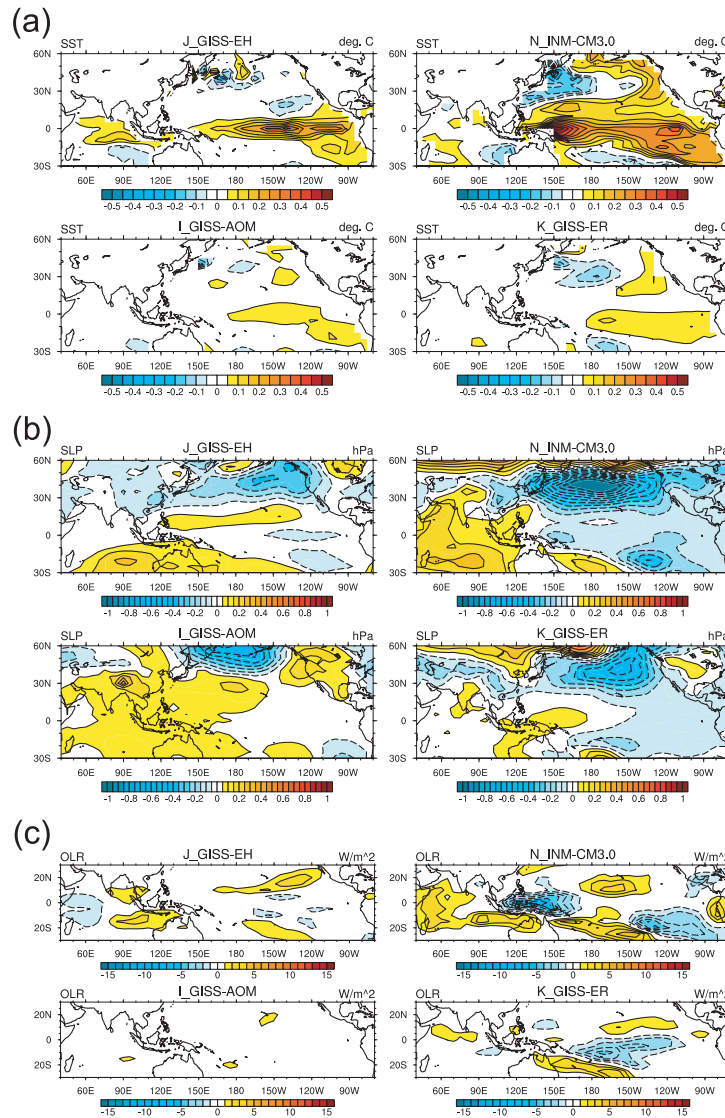


Fig. 13. Same as in Fig. 6, but for the four models with the low PDO metric (Models I, N, J and K) in the AIB simulations.

M, respectively. In association with this SSTA pattern, the regressed SLP anomalies show a zonal dipole in the tropics and a negative center of action in the eastern North Pacific in these five models (Fig. 12b) as shown in Fig. 7b for the 20C3M simulations. Likewise, the negative (positive) OLR anomalies in the central (western) tropical Pacific are similar to the observed pattern over the 20th century (Fig. 12c). In contrast, while the four models with the low PDO metric simulate the basin-scale warming over the tropical Pacific (Fig. 13a), the SLP (Fig. 13b) and OLR (Fig. 13c) anomalies

over the tropical Pacific are weak (Models J, K and I) or locate at an inappropriate area (Models N), compared to the observations.

As examined for the 20C3M simulations, the zonal variations of SST, SLP and OLR anomalies over the tropical Pacific for the AIB simulations are plotted in Fig. 14. In the Models M, V, W, T and Q with the high PDO metric, those zonal variations are similar to those in the observed over the 20th century (Figs. 14a, c, e). Specifically, the negative OLR anomalies in the Model Q in the AIB simulation become significant and are almost twice

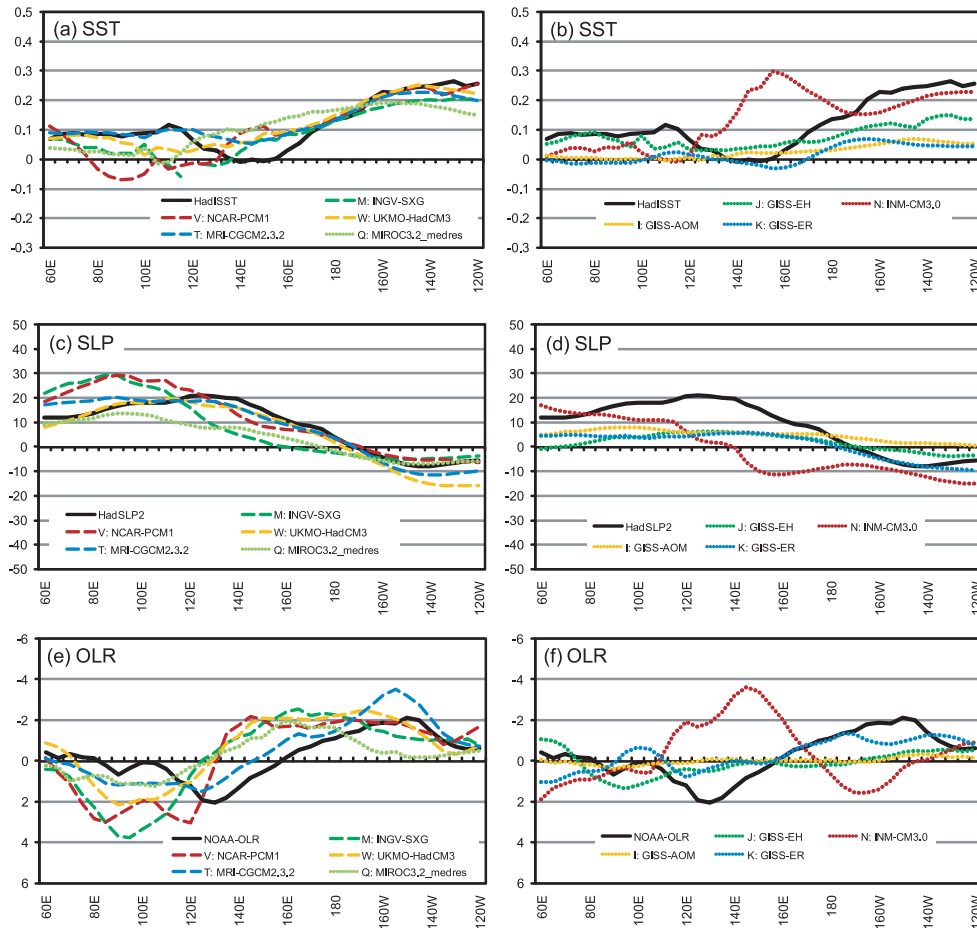


Fig. 14. Same as in Fig. 9, but for the A1B simulations. The plot of the Model Q is moved into the left panels.

as much as in the 20C3M simulations. Meanwhile, the tropical SLP and OLR anomalies in the Models J, N, K and I with the low PDO metric are largely different from the observations (Figs. 14b, d, f). These results suggest that the high PDO metric in the Models M, V, W, T and Q is given by the fact that the zonal variations of the tropical ocean and atmosphere in the A1B simulations are simulated as observed over 20th century.

5. Summary

Reproducibility of the PDO is evaluated for the 20C3M simulations in the 24 CMIP3 models, based on the PDO metric in the Taylor diagram and temporal correlation coefficient R_t between the PDO and decadal-ENSO indices. The PDO metric for the 20C3M simulations is high in the five Models M, V, Q, W and T (greater than 0.67) and low

in the four Models J, N, I and K (less than 0.41). Among the five models with the high PDO metric, the four models (Models M, T, V and W) with significant correlation R_t indicate the tropics-extratropics linkage, while the Model Q failed to reproduce the linkage. The R_t in the four models with the low PDO metric (Models J, N, I and K) is not so high as in the four models with the high PDO metric. This indicates that the high reproducibility of the tropics-extratropics linkage in the decadal SST variability plays some roles for the high PDO metric in the 20C3M simulations.

The models with the high PDO metric and significant correlation R_t (Models M, V, W and T) mostly reproduce natural climate variation on the decadal timescales in the Pacific. Associated with the warm (cold) phase of the decadal-ENSO, the negative (positive) SSTAs with the horseshoe-like

pattern and negative (positive) SLP anomalies are reproduced in the North Pacific, while the zonal dipole of SLP anomalies with negative (positive) in the east and positive (negative) in the west, and negative (positive) OLR anomalies over the tropical Pacific. These results indicate successful simulation of the tropical climate variations over the 20th century, where weakened (enhanced) Walker circulation over the basin-scale SST warming (cooling) induces the atmospheric teleconnection pattern that acts to form strong (weak) westerlies over the North Pacific and thereby enhance (weaken) cooling of the ocean surface, as revealed in the observational analysis (Nitta and Yamada 1989; Trenberth 1990; Zhang et al. 1997). In contrast, the models with the weak correlation R_t (Models, J, N, K, I and Q) fail to reproduce the realistic SST, OLR and SLP anomalies associated with the decadal-ENSO. Thus, the PDO reproducibility needs realistic tropics-extratropics linkage via the atmospheric teleconnection induced by the decadal SST variation in the tropical Pacific.

In the 21st century, while the SSTAs in the North Pacific in the A1B simulations show a pronounced warming trend, they still represent variations on the decadal timescales. The models with the high PDO metric in the 20C3M simulations tend to simulate the observed PDO pattern in the A1B simulations, which is consistent with the results by Overland and Wang (2007). This is because the tropical SST, SLP and OLR anomalies associated with the simulated decadal-ENSO index are still similar to the observed pattern even in the A1B simulations. Meanwhile, the models with the low PDO metric in the 20C3M simulations still failed to simulate the observed PDO pattern in the A1B simulations probably because the tropical anomalies are largely different from those in the observation. However, these results are not able to guarantee that the horseshoe-like pattern of the Pacific SSTA field would be formed in the natural future climate. Rather, it is a model property that tends to simulate the natural climate variations with observed patterns under the global warming condition.

Acknowledgments

The authors would like to thank the editor, Dr. S. Yukimoto, and two anonymous reviewers for their useful comments. This work is supported by the Global Environment Research Fund (S-5-2) of the Ministry of the Environment, Japan. We acknowledge the modeling groups, the Program for

Climate Model Diagnosis and Intercomparison (PCMDI) and the WCRP's Working Group on Coupled Modeling (WGCM) for their roles in making available the WCRP CMIP3 multi-model dataset. Support of this dataset is provided by the Office of Science, U.S. Department of Energy. We also express our gratitude to the "Data Integration and Analysis System" Fund for National Key Technology from the Ministry of Education, Culture, Sports, Science and Technology, Japan, for providing us with an invaluable environment for a mass data handling. NCAR Command Language (NCL) and Ferret software developed at NOAA/PMEL were used for analysis and drawing figures.

References

- AchutaRao, K. M., and K. R. Sperber, 2006: ENSO Simulation in Coupled Ocean-Atmosphere Models: Are the Current Models Better?. *Clim. Dyn.*, **27**, 1–15, doi:10.1007/s00382-006-0119-7.
- Alexander, M. A., I. Bladé, M. Newman, J. R. Lanzante, N. C. Lau, and J. D. Scott, 2002: The Atmospheric Bridge: The Influence of ENSO Teleconnections on Air-Sea Interaction over the Global Oceans. *J. Climate*, **15**, 2205–2231.
- Allan, R., and T. Ansell, 2006: A new globally-complete monthly historical gridded mean sea level pressure data set (HadSLP2): 1850–2003. *J. Climate*, **19**, 5816–5842.
- Burgman, R. J., A. C. Clement, C. M. Mitos, J. Chen, and K. Esslinger, 2008: Evidence for atmospheric variability over the Pacific on decadal timescales. *Geophys. Res. Lett.*, **35**, L01704, doi:10.1029/2007GL031830.
- Deser, C., A. S. Phillips, and J. W. Hurrell, 2004: Pacific Interdecadal Climate Variability: Linkages between the Tropics and the North Pacific during Boreal Winter since 1900. *J. Climate*, **17**, 3109–3124.
- IPCC, 2001: *Climate Change 2001: The Scientific Basis. Contribution of Working Group I to the Third Assessment Report of the Intergovernmental Panel on Climate Change* [Houghton, J. T., Y. Ding, D. J. Griggs, M. Noguer, P. J. van der Linden, X. Dai, K. Maskell, and C. A. Johnson (eds.)]. Cambridge University Press, 881 pp.
- IPCC, 2007: *Climate Change 2007: The Physical Science Basis. Contribution of Working Group I to the Fourth Assessment Report of the Intergovernmental Panel on Climate Change* [Solomon, S., D. Qin, M. Manning, Z. Chen, M. Marquis, K. B. Averyt, M. Tignor and H. L. Miller (eds.)]. Cambridge University Press, 996 pp.
- Kusunoki, S., J. Yoshimura, H. Yoshimura, A. Noda, K. Oouchi, and R. Mizuta, 2006: Change of Baiu rain

- band in global warming projection by an atmospheric general circulation model with a 20-km grid size. *J. Meteor. Soc. Japan*, **84**, 581–611.
- Latif, M., and T. P. Barnett, 1994: Cause of decadal climate variability over the North Pacific and North America. *Science*, **266**, 634–637.
- Lau, N. C., 1997: Interactions between Global SST Anomalies and the Midlatitude Atmospheric Circulation. *Bull. Amer. Meteor. Soc.*, **78**, 21–33.
- Liebmann, B., and C. A. Smith, 1996: Description of a Complete (Interpolated) Outgoing Longwave Radiation Dataset. *Bull. Amer. Meteor. Soc.*, **77**, 1275–1277.
- Mantua, N. J., and S. R. Hare, 2002: The Pacific Decadal Oscillation. *J. Oceanography*, **58**, 35–44.
- Meehl, G. A., C. Covey, T. Delworth, M. Latif, B. McAvaney, J. F. B. Mitchell, R. J. Stouffer, and K. E. Taylor, 2007: The WCRP CMIP3 multimodel dataset: A new era in climate change research. *Bull. Amer. Meteor. Soc.*, **88**, 1383–1394, doi:10.1175/BAMS-88-9-1383.
- Nakamura, H., G. Lin, and T. Yamagata, 1997: Decadal Climate Variability in the North Pacific during the Recent Decades. *Bull. Amer. Meteor. Soc.*, **78**, 2215–2225.
- Nitta, T., and S. Yamada, 1989: Recent warming of tropical sea surface temperature and its relationship to the Northern Hemisphere circulation. *J. Meteor. Soc. Japan*, **67**, 187–193.
- Nonaka, M., H. Nakamura, Y. Tanimoto, T. Kagimoto, H. Sasaki, 2006: Decadal variability in the Kuroshio-Oyashio Extension simulated in an eddy-resolving OGCM. *J. Climate*, **19**, 1970–1989.
- Nozawa, T., T. Nagashima, H. Shiogama, and S. A. Crooks, 2005: Detecting natural influence on surface air temperature change in the early twentieth century. *Geophys. Res. Lett.*, **32**, L20719, doi:10.1029/2005GL023540.
- Overland, J. E., and M. Wang, 2007: Future climate of the North Pacific Ocean. *Eos Trans. AGU*, **88**, 178, 182.
- Rayner, N. A., D. E. Parker, E. B. Horton, C. K. Folland, L. V. Alexander, D. P. Rowell, E. C. Kent, and A. Kaplan, 2003: Global Analyses of SST, Sea Ice and Night Marine Air Temperature Since the Late 19th Century. *J. Geophys. Res.*, **108**, 4407, doi:10.1029/2002JD002670
- Santer, B. D., C. Mears, F. J. Wentz, K. E. Taylor, P. J. Gleckler, T. M. L. Wigley, T. P. Barnett, J. S. Boyle, W. Bruggemann, N. P. Gillett, S. A. Klein, G. A. Meehl, T. Nozawa, D. W. Pierce, P. A. Stott, W. M. Washington, and M. F. Wehner, 2007: Identification of human-induced changes in atmospheric moisture content. *Proc. Nat. Acad. Sci.*, **104**, 15248–15253.
- Schneider, N., A. J. Miller, and D. W. Pierce, 2002: Anatomy of North Pacific decadal variability. *J. Climate*, **15**, 586–605.
- Tanimoto, Y., H. Nakamura, T. Kagimoto, and S. Yamane, 2003: An active role of extratropical sea surface temperature anomalies in determining anomalous turbulent heat flux. *J. Geophys. Res.*, **108**, 3304, doi:10.1029/2002JC001750.
- Taylor, K. E., 2001: Summarizing multiple aspects of model performance in a single diagram. *J. Geophys. Res.*, **106**, 7183–7192.
- Tett, S. F. B., P. A. Stott, M. R. Allen, W. J. Ingram, and J. F. B. Mitchell, 1999: Causes of twentieth-century temperature change near the Earth's surface. *Nature*, **399**, 569–572.
- Trenberth, K. E., 1990: Recent observed interdecadal climate changes in the Northern Hemisphere. *Bull. Amer. Meteor. Soc.*, **71**, 988–993.
- Trenberth, K. E., 1997: The Definition of El Niño. *Bull. Amer. Meteor. Soc.*, **78**, 2771–2777.
- Trenberth, K. E., and J. W. Hurrell, 1994: Decadal atmosphere-ocean variations in the Pacific. *Clim. Dyn.*, **9**, 303–319.
- Wu, L., Z. Liu, R. Gallimore, R. Jacob, D. Lee, and Y. Zhong, 2003: Pacific Decadal Variability: The Tropical Pacific Mode and the North Pacific Mode. *J. Climate*, **16**, 1101–1120.
- Zhang, Y., J. M. Wallace, and D. S. Battisti, 1997: ENSO-like Interdecadal Variability: 1900–93. *J. Climate*, **10**, 1004–1020.
- Zhang, X., F. W. Zwiers, G. C. Hegerl, F. H. Lambert, N. P. Gillett, S. Solomon, P. A. Stott, and T. Nozawa, 2007: Detection of human influence on twentieth-century precipitation trends. *Nature*, **448**, 461–465.